Article

Electrolyte design for Li-ion batteries under extreme operating conditions

Jijian Xu[1], Jiaxun Zhang[1], Travis P. Pollard[2], Qingdong Li[3], Sha Tan[4], Singyuk Hou[1], Hongli Wan[1], Fu Chen[5], Huixin He[3], Enyuan Hu[4], Kang Xu[2], Xiao-Qing Yang[4], Oleg Borodin[2✉] & Chunsheng Wang[1✉]

The ideal electrolyte for the widely used $LiNi_{0.8}Mn_{0.1}Co_{0.1}O_2$ (NMC811)∥graphite lithium-ion batteries is expected to have the capability of supporting higher voltages (≥4.5 volts), fast charging (≤15 minutes), charging/discharging over a wide temperature range (±60 degrees Celsius) without lithium plating, and non-flammability[1–4]. No existing electrolyte simultaneously meets all these requirements and electrolyte design is hindered by the absence of an effective guiding principle that addresses the relationships between battery performance, solvation structure and solid-electrolyte-interphase chemistry[5]. Here we report and validate an electrolyte design strategy based on a group of soft solvents that strikes a balance between weak Li^+–solvent interactions, sufficient salt dissociation and desired electrochemistry to fulfil all the aforementioned requirements. Remarkably, the 4.5-volt NMC811∥graphite coin cells with areal capacities of more than 2.5 milliampere hours per square centimetre retain 75 per cent (54 per cent) of their room-temperature capacity when these cells are charged and discharged at −50 degrees Celsius (−60 degrees Celsius) at a C rate of 0.1C, and the NMC811∥graphite pouch cells with lean electrolyte (2.5 grams per ampere hour) achieve stable cycling with an average Coulombic efficiency of more than 99.9 per cent at −30 degrees Celsius. The comprehensive analysis further reveals an impedance matching between the NMC811 cathode and the graphite anode owing to the formation of similar lithium-fluoride-rich interphases, thus effectively avoiding lithium plating at low temperatures. This electrolyte design principle can be extended to other alkali-metal-ion batteries operating under extreme conditions.

State-of-the-art electrolytes based on carbonate esters fail to meet most of the requirements for extreme lithium (Li)-ion batteries (LIBs) because their voltage window is limited to 4.3 V, they have a narrow operating temperature range of −20 °C to +50 °C and they are highly flammable[5]. Enabling low-temperature operation has been achieved previously by reducing the freezing point of the electrolyte through the introduction of a series of co-solvents with a low freezing point, such as linear carboxylate esters and ethers[6,7]. However the narrower electrochemical stability of these esters and ethers of 1.5–4.7 V (versus Li^+/Li) sets an upper limit on the battery voltage[8]. Recent breakthroughs in low-temperature batteries via liquefied gas electrolytes are able to retain more than 60% of room-temperature capacity even at −60 °C (ref. [9]), but the low boiling point of these volatile solvents requires hermetical cell redesign under pressures needed for gas liquefaction.

In addition to ionic conductivity, the interfacial/interphasial resistance dominates at low temperatures, which requires electrolytes to have low Li^+ desolvation energy[10,11]. Owing to the joint effects of large charge transfer and low ion conductivity below −20 °C, high overpotentials reduce the accessible capacity and lead to Li^0 plating on the graphite surface[12,13]. Li^0 plating on graphite accelerates capacity decay and reduces the Coulombic efficiency (CE) to below 99.5%. Furthermore, Li dendrite growth may short the cell, which presents a safety hazard[14]. To circumvent Li^0 plating on graphite at low temperatures, a common practice is to use a relatively high negative/positive (N/P) capacity ratio in commercial LIBs, which ensures better safety at the expense of overall energy density[15]. However, Li dendrites may still occur under fast charging or extremely low temperatures (less than −20 °C) because the charge/discharge kinetics between the graphite anode and the NMC811 cathode are different. As the charge/discharge kinetics of the electrodes are largely controlled by the interphases, an ideal low-temperature electrolyte should form kinetically matched interphases on both electrodes to achieve low and equivalent overpotentials at different temperatures and currents.

Balanced electrolyte design principle

A low freezing point but a moderate boiling point and a wide electrochemical stability window set the primary criteria for solvent selection

[1]Department of Chemical and Biomolecular Engineering, University of Maryland, College Park, MD, USA. [2]Battery Science Branch, Army Research Directorate, US DEVCOM Army Research Laboratory, Adelphi, MA, USA. [3]Department of Chemistry, Rutgers, The State University of New Jersey, Newark, NJ, USA. [4]Chemistry Division, Brookhaven National Laboratory, Upton, NY, USA. [5]Department of Chemistry and Biochemistry, University of Maryland, College Park, MD, USA. ✉e-mail: oleg.a.borodin.civ@army.mil; cswang@umd.edu

Article
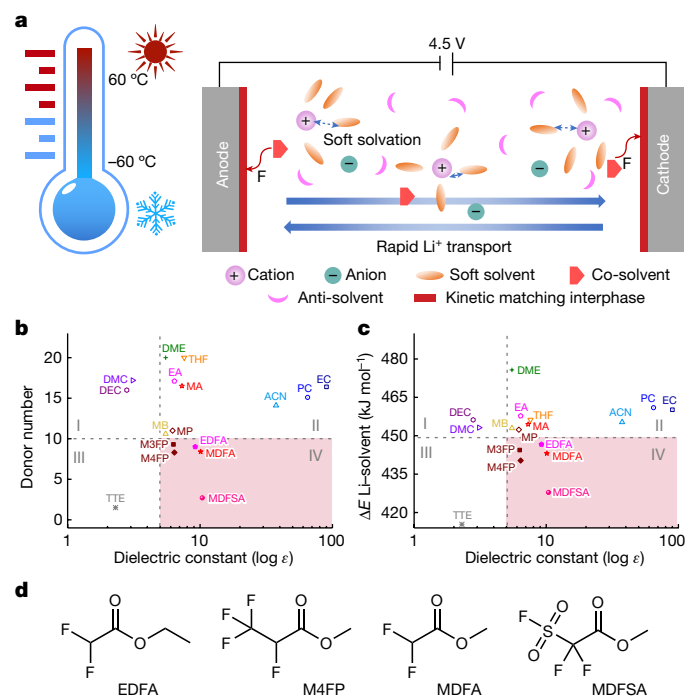
Fig. 1 | Electrolyte design strategies. a, Illustration of the soft solvation between the soft solvent and Li ions, rapid Li-ion transport and wide-temperature-range (±60 °C) stability. **b**, The solvent diagram of DN versus dielectric constant. Solvents located in zone IV are denoted as soft solvents, in which the lower DN and higher dielectric constant effectively reduce the Li$^+$–solvent affinity without sacrificing kinetic transportation. **c**, The Li$^+$–solvent binding energy from DFT calculations versus experimental dielectric constant. ACN, acetonitrile; DMC, dimethyl carbonate; DME, dimethoxyethane; EA, ethyl acetate; EC, ethylene carbonate; MB, methyl butyrate; MP, methyl propionate; PC, propylene carbonate; THF, tetrahydrofuran. **d**, Chemical structure of the soft solvating solvents.

(Extended Data Table 1), and the secondary criteria should be a soft solvating ability that ensures a low Li$^+$-ion desolvation energy with little sacrificing of ionic dissociation ability (Fig. 1a). The donor number (DN) and Li$^+$–solvent binding energy from density functional theory (DFT) calculations reveal a close correlation between them (Fig. 1b,c and Supplementary Discussion 1), making DFT a useful method for screening solvating ability. Most known polar solvents with a high salt dissociating ability have a high DN (>10) (zones I and II in Fig. 1b)[16,17], whereas those with a low DN and low dielectric constant have a poor salt dissociating ability (zone III in Fig. 1b,c), representing non-solvating diluents. However, there appears to be a balanced region (zone IV) comprising low-DN solvents with moderate dielectric constants that lead to modest Li$^+$–solvent binding energies and salt dissociation.

Applying these two criteria to a number of solvents (Fig. 1a–c), a family of fluorinated esters (ethyl difluoroacetate (EDFA), methyl 2,3,3,3-tetrafluoro propionate (M4FP), methyl difluoroacetate (MDFA) and methyl 2,2-difluoro-2 (fluorosulfonyl)acetate (MDFSA); chemical structures illustrated in Fig. 1d) were identified as prime candidates. One of the zone IV solvents methyl (3,3,3-trifluoropionate) (M3FP) has previously shown promising results in Li-metal batteries under a low temperature of −60 °C (ref. [18]), providing additional support for the proposed criteria. Compared against non-fluorinated ester solvents, the fluorinated counterparts (MDFA, EDFA and M4FP) have a wider electrochemical stability window, greater thermal stability and ultralow freezing points (Extended Data Table 1)[19,20].

To maximize ionic conductivity, soft solvents need to be coupled with highly dissociating and solvable lithium salt. A study of (glyme)–LiX electrolytes showed that salt dissociation follows the order:

lithium bis(trifluoromethanesulfonyl)imide (LiTFSI) > LiClO$_4$, LiI > LiBF$_4$ > LiCF$_3$SO$_3$ > LiNO$_3$, LiBr > LiCF$_3$CO$_2$ (ref. [21]), which is consistent with the DN values of some of the anions (TFSI$^-$, 5.4; CF$_3$SO$_3^-$, 16.9; Br$^-$, 33.7). LiTFSI is a good choice owing to a weak Li$^+$ binding energy[22,23], and a high solubility of 5.0 M, 4.5 M and 3.0 M in MDFA, EDFA and M4FP solvents, respectively.

Soft solvating solvents also promote the formation of a lithium fluoride (LiF)-rich solid−electrolyte interphase (SEI) and cathode−electrolyte interphase (CEI) owing to the high reduction potentials observed in DFT screening of the solvent and Li$^+$–solvent complexes (Supplementary Discussion 2). These solvents intrinsically favour the formation of prevailing ion pairs and aggregates in the solution, which is beneficial for forming anion-derived LiF-rich interphases. MDFSA (fluorosulfonyl substituted MDFA; molecular structure shown in Fig. 1d) with a high reduction potential of 2.2 V was added as a co-solvent to further reduce the solvation degree of Li$^+$ and to enhance the formation of LiF-rich SEI and LiF-rich CEI. The addition of 1,1,2,2-tetrafluoroethyl-2,2,3,3-tetrafluoropropylether (TTE) diluent renders the electrolyte non-flammable when the volume ratio of TTE in the mixture solvent exceeds 40%.

Both the graphite anode and the LiNi$_{0.8}$Mn$_{0.1}$Co$_{0.1}$O$_2$ (NMC811) cathode experience relatively small volume change during lithiation/delithiation, which can be tolerated by the elastic inorganic−organic interphase, leading to excellent cycle life (Extended Data Fig. 1a)[24]. As the organic interphase has higher activation energy, higher electronic conductivity, higher solubility in electrolyte and lower high-voltage stability than LiF, it is still desirable to minimize the organic content in the interphase. Increasing the LiF content is expected to reduce the thickness of the SEI during its self-limiting formation process, leading to lower area-specific resistance even at a low temperature (Extended Data Fig. 1b). The similar LiF-rich compositions of both the SEI and the CEI also improve the overpotential, capacity and kinetics matching between the graphite anode and the NMC811 cathode at different currents and temperatures (Extended Data Fig. 1d), allowing maximum cell capacity and Li^0 plating prevention by controlling the cell voltage (Extended Data Fig. 1e)[25]. In comparison, the inorganic−organic SEI/CEI formed in conventional carbonate electrolytes results in mismatched capacities and overpotentials between the anode and cathode (Extended Data Fig. 1c), thus affecting the high-rate and low-temperature performance of the full cells. Balancing the thermodynamic (capacity) and kinetic (interface resistance) matching between the graphite anode and NMC811 cathode effectively suppresses Li^0 plating during fast charging at room temperature and operation at low temperatures. The high-modulus, lithiophobic LiF-rich interphases mitigate lithium dendrite growth even if locally Li^0 plating happens under extreme conditions.

Physicochemical properties and solvation structure

After dissolving LiTFSI into different solvents, the TFSI$^-$···Li$^+$ coordination was characterized using Raman spectroscopy[26]. Among all the electrolytes with commonly used solvents, the TFSI$^-$ anion peak corresponding to S–N–S bending/vibration in 1 M LiTFSI−MDFA electrolyte produces the smallest redshift (2 cm^{-1}; Fig. 2a) when referenced against crystalline LiTFSI (748.5 cm^{-1}), indicating that MDFA has the lowest solvation ability[27]. The increase of LiTFSI salt concentration and addition of TTE further reduce the Li$^+$–solvent coordination, resulting in higher population of ionic aggregation (Supplementary Discussion 3). The solvation structures of the electrolytes with different solvents (methyl acetate (MA), EDFA, MDFA and M4FP) were also investigated using nuclear magnetic resonance (NMR). The smallest Δδ of 2.0 ppm for M4FP (Fig. 2b) is directly related to the weakest Li$^+$–solvent interaction, consistent with the DN value (Supplementary Discussion 4)[28].

The ionic conductivity of the prepared soft electrolytes is summarized in Fig. 2c. As expected, the ionic conductivity is the lowest for the M4FP-based electrolyte as it has the lowest DN and dielectric constant. At 20 °C, the ionic conductivities of the proposed soft electrolytes are
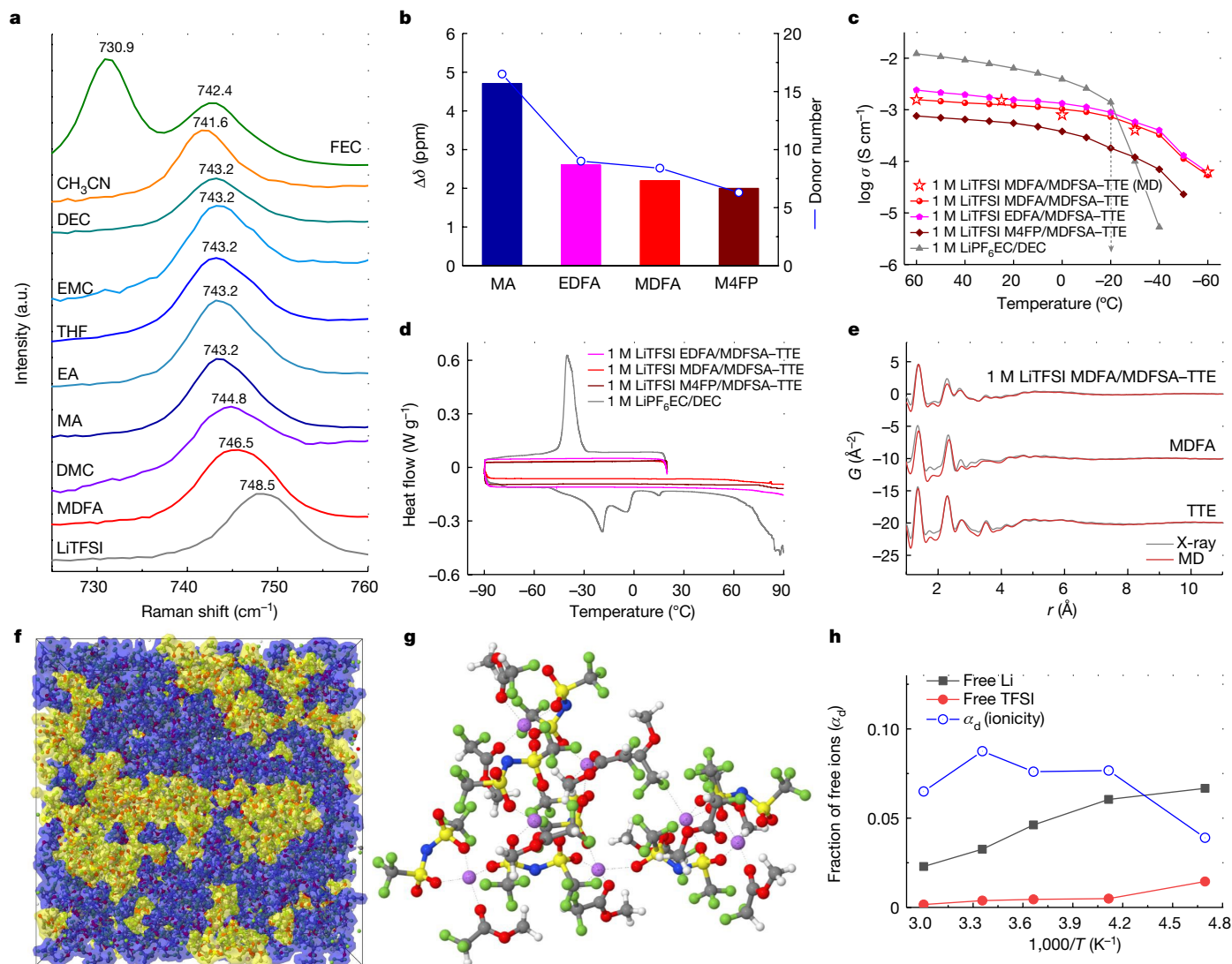
Fig. 2 | Physical properties of the electrolytes. a, Raman spectra of 1 M LiTFSI in different solvents. **b**, Summary of $\Delta\delta$ (^{13}C NMR spectra of carbonyl carbons) in different solvents with and without LiTFSI. **c**, Temperature dependence of the conductivity of different electrolytes. For comparison, red stars represent conductivity values predicted with MD. **d**, DSC cooling and heating curves of different electrolytes. **e**, PDF data of 1 M LiTFSI MDFA/MDFSA–TTE electrolyte, and single solvents. Grey line, experiment data; red line, MD simulation predictions. **f**–**h**, MD simulation results. **f**, A snapshot of the simulation box of 1 M MDFA/MDFSA–TTE. LiTFSI–MDFA is highlighted by the yellow isosurface, and TTE and MDFSA are highlighted by the blue isosurface. **g**, Representative ionic aggregates from MD simulation at 25 °C. Jmol colour schemes are used: Li, purple; N, blue; F, green; S, yellow; C, grey; O, red; H, white. **h**, Fraction of free Li$^+$ and TFSI$^-$ defined as the ions not coordinated to any counterion within 5.0 Å of Li–N(TFSI), and degree of dynamics uncorrelated motion a_d (ionicity) from MD simulations of 1 M LiTFSI in MDFA/MDFSA–TTE electrolyte.

1.8 mS cm^{-1} for EDFA, 1.7 mS cm^{-1} for MDFA and 0.6 mS cm^{-1} for M4FP, which are slightly lower than that of EC/DEC electrolyte (6.4 mS cm^{-1}). However, at temperatures below −20 °C, the ionic conductivities of MDFA-based electrolytes outperform that of EC/DEC electrolytes (Fig. 2c). The sudden drop in the ionic conductivity of ethylene carbonate/diethylene carbonate (EC/DEC) electrolyte around −20 °C is due to solidification of the electrolyte. This phase transition of the EC/DEC electrolyte was identified through differential scanning calorimetry (DSC) (Fig. 2d), exhibiting two observable endothermic peaks around −4.0 °C and −18.6 °C. DSC also demonstrated that none of the soft solvent-based electrolytes undergo a phase change over the temperature range of −90 °C to +90 °C (Supplementary Discussion 5). Taking all the above factors, including Li$^+$–solvent binding energy, ionic conductivity and electrochemical stability window, into account, 1 M LiTFSI MDFA/MDFSA–TTE soft electrolyte is selected for further study.

The solvation structure of 1 M LiTFSI MDFA/MDFSA–TTE electrolyte was further analysed using X-ray pair distribution function (PDF). The experimental results agreed well with molecular dynamics (MD) simulations both in real (R) space (Fig. 2e) and scattering vector (Q) space (Extended Data Fig. 2a,b), validating the MD simulation predictions of the electrolyte structure. Snapshots of MD simulation boxes (Fig. 2f and Extended Data Fig. 3a,b) indicate that the addition of TTE and MDFA promotes ion aggregation. In the mixed MDFA/MDFSA–TTE solvent electrolyte, the Li$^+$ are primarily coordinated by 1.92 MDFA and 1.66 TFSI$^-$ anions with a minor contribution of 0.09 from MDFSA (Fig. 2g). Free Li$^+$-ions solvent separated from TFSI$^-$ are primarily coordinated by 4 MDFA (Extended Data Fig. 3c). In 1 M LiTFSI in MDFA, 10% of free Li$^+$ and 3% of free TFSI$^-$ were observed at room temperature. Dilution with TTE and MDFSA decreased the fraction of free Li$^+$ to 2–7% depending on temperature, and the fraction of free TFSI$^-$ was below 0.4%, indicating that nearly all TFSI$^-$ anions are participating in aggregates (Fig. 2f and Supplementary Discussion 6). Decreasing the temperature slightly increases the fraction of free Li$^+$ whereas ionicity (inverse Haven ratio) stays approximately the same and even slightly decreases below −30 °C
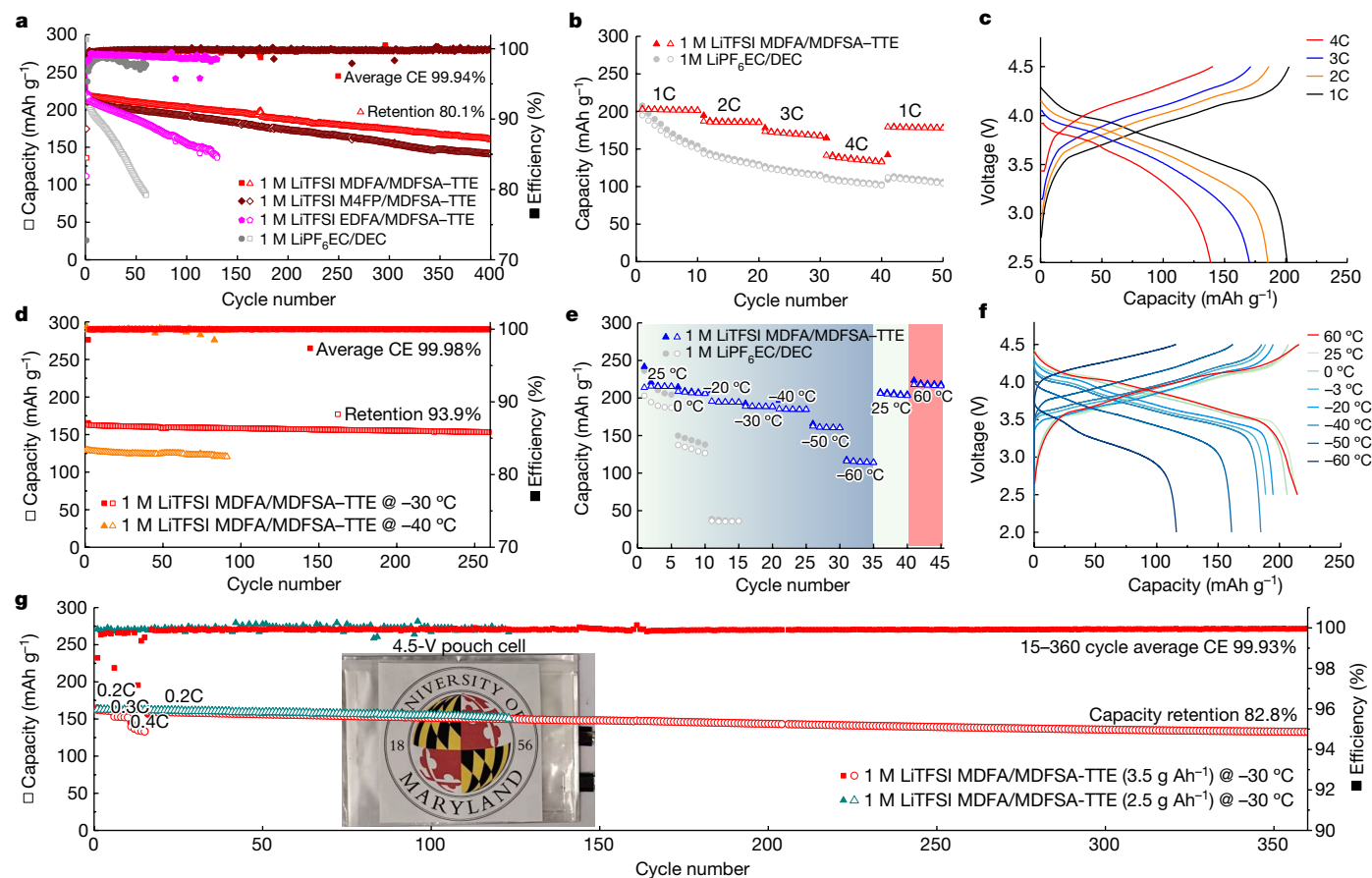
Fig. 3 | Electrochemical performance of NMC811||graphite full cells.
a, Cycling performance at 0.5C under 25 °C. **b,c**, Rate performance at 25 °C (**b**) and corresponding voltage profiles (**c**). **d–f**, Long cycling performance at 0.2C under −30 °C/−40 °C (**d**), cycling performance at 0.1C under different temperatures (60 °C, 25 °C, 0 °C, −20 °C, −30 °C, −40 °C, −50 °C and −60 °C) (**e**) and corresponding voltage profiles of cells in **e** using 1 M LiTFSI MDFA/ MDFSA–TTE electrolyte (**f**). **g**, Pouch cell performance at −30 °C and rate of 0.2C using 2.5 g Ah⁻¹ or 3.5 g Ah⁻¹ electrolytes. Rate performance was conducted using the cell with electrolyte of 3.5 g Ah⁻¹ (red) at different C rates (0.2C for 5 cycles, 0.3C for 5 cycles, 0.4C for 5 cycles and 0.2C for 345 cycles). Inset: photo of a 4.5-V pouch cell.

(Fig. 2h), resulting in a more pronounced decrease of conductivity in this region (Extended Data Fig. 3d,e).

Electrochemical performance of 4.5-V NMC811||graphite full cells

Figure 3a shows that the performance of full cells in the 1 M LiTFSI MDFA/MDFSA–TTE electrolytes outperform EC/DEC-based electrolyte. Specifically, the full cell in 1 M LiTFSI MDFA/MDFSA–TTE electrolyte shows a capacity retention of 80.1% after 400 cycles with an average CE of 99.94% (Supplementary Discussion 7). Improvements in rate performance over 1 M LiPF$_6$ EC/DEC are shown in Fig. 3b for NMC811||graphite full cells with the 1 M LiTFSI MDFA/MDFSA–TTE electrolyte, delivering a capacity of 202 mAh g⁻¹ at 1C, 185 mAh g⁻¹ at 2C, 169 mAh g⁻¹ at 3C and 140 mAh g⁻¹ at 4C (here, the C rate is determined by the charging time, with 1C being equal to 1 h and so on). The corresponding charge/ discharge voltage profiles of the cells at different C rates with 1 M LiTFSI MDFA/MDFSA–TTE are shown in Fig. 3c. The rate performance is further improved by adopting polycrystalline NMC811, demonstrating stable cycling performance of NMC811||graphite pouch cells with lean electrolytes at a high rate of 3–4C (Extended Data Fig. 4). Moreover, capacity is matched between the graphite anode and NMC811 cathode at different C rates (Supplementary Discussion 8).

In addition to the excellent performance at room temperature, NMC811||graphite full cells also exhibited exceptional performance at low temperatures. Figure 3d shows the cycling stability of NMC811||graphite full cells with 1 M LiTFSI MDFA/MDFSA–TTE electrolytes at 0.2C at −30 °C and −40 °C. At −30 °C, 93.9% of capacity is retained after 260 cycles with an average CE of 99.98%. At lower temperatures down to −50 °C/−60 °C, a slightly faster capacity decay is observed (Extended Data Fig. 5). Figure 3e compares the performance of NMC811||graphite full cells in two electrolytes at different temperatures. The NMC811||graphite full cells with the EC/DEC electrolyte fail to operate at −30 °C owing to the solidification of the electrolyte. In contrast, the capacity of the NMC811||graphite full cell with 1 M MDFA/MDFSA–TTE electrolyte shows high retention of their room-temperature capacity at low temperature: 206.8 mAh g⁻¹ (95%), 194.5 mAh g⁻¹ (90%), 188.7 mAh g⁻¹ (87%), 184.6 mAh g⁻¹ (85%), 161.0 mAh g⁻¹ (75%) and 115.5 mAh g⁻¹ (54%) when cycled at 0 °C, −20 °C, −30 °C, −40 °C, −50 °C and −60 °C, respectively. Representative voltage curves of full cells with 1 M LiTFSI MDFA/MDFSA–TTE electrolyte at different temperatures are shown in Fig. 3f. NMC811||graphite full cells with 1 M MDFA/MDFSA–TTE electrolyte can fully restore their original capacity at 25 °C even after ultralow-temperature operation at −60 °C, suggesting LiF-rich interphases are robust enough to mitigate Li⁰ plating and dendrites.

To better represent practical conditions, NMC811||graphite pouch cells were evaluated (Fig. 3g) and delivered a charge/discharge capacity of 160.2 mAh g⁻¹ at 0.2C under −30 °C, which is similar to that of coin cells under the same conditions. No obvious capacity decay is observed even with a lean electrolyte of 2.5 g Ah⁻¹ (Fig. 3g). At higher C rates of 0.4C and 0.5C, the pouch cell shows capacities of 152.6 mAh g⁻¹
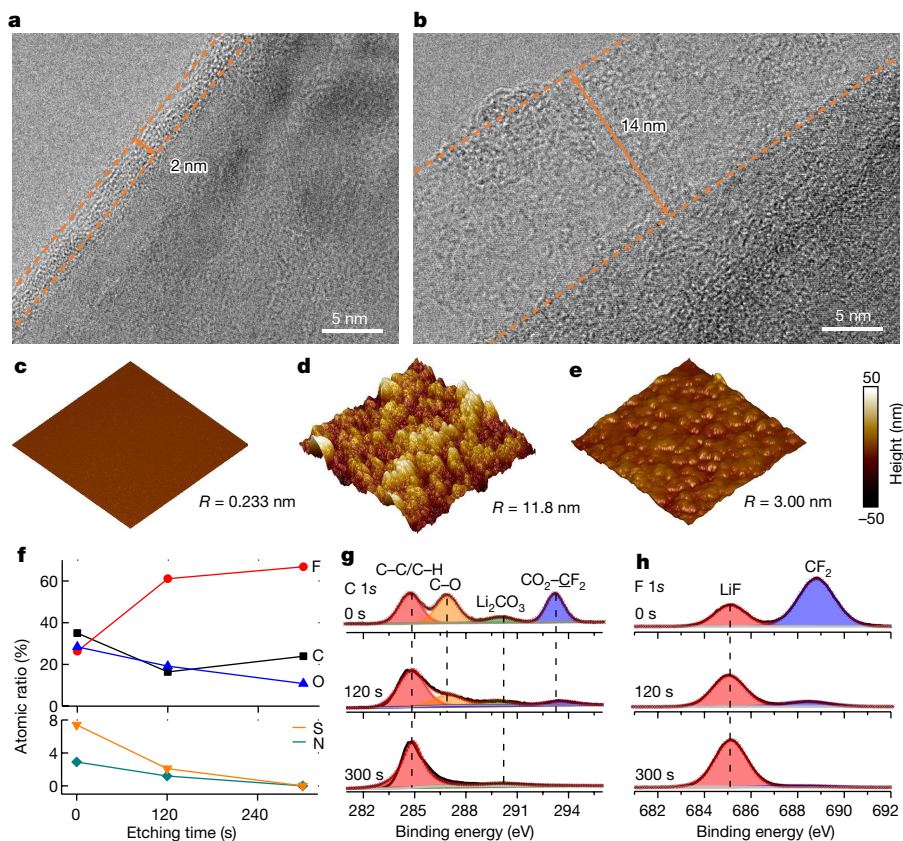
Fig. 4 | Characterization of SEI layers on graphite anode after cycling at −30 °C. a,b, HRTEM images with 1 M LiTFSI MDFA/MDFSA–TTE electrolyte (**a**) and 1 M LiPF₆ EC/DEC electrolyte (**b**). The orange dashed lines are used to outline the SEI on the cycled graphite anode. **c–e**, Morphology of the graphite electrode before (**c**) and after (**d**) cycling in 1 M LiPF₆ EC/DEC electrolyte, and

1 M LiTFSI MDFA/MDFSA–TTE electrolyte (**e**). AFM roughness (*R*) comparison on an area of 0.5 μm × 0.5 μm. **f–h**, XPS results of the SEI on cycled graphite in 1 M LiTFSI MDFA/MDFSA–TTE electrolyte: quantified atomic ratios of the elements in SEI (**f**), and C 1*s* (**g**) and F 1*s* (**h**) spectra displayed in columns of the corresponding depth profiling results.

and 134.6 mAh g⁻¹, respectively. NMC811‖graphite pouch cells maintained 80% capacity after 360 cycles. Conducting both the charging and discharging test of the pouch cell at the same low temperature is a very aggressive protocol, especially at very low temperatures with normal 0.2–0.3C rates (Supplementary Discussion 9)[29–31]. In addition to exceptional low-temperature performance, 1 M MDFA/MDFSA–TTE electrolyte also showed that NMC811‖graphite full cells achieved an improved capacity at a high temperature as the formed LiF-rich SEI and CEI are less soluble in the electrolyte (Supplementary Discussion 10)[32,33].

To quantitatively analyse the improved low-temperature performance, three-electrode pouch cells were used to simultaneously monitor the behaviour of the anode and cathode (Extended Data Fig. 6a), in which the voltage of the cell (*U*), the potential of the NMC811 cathodes (*E*(+)) and the potential of the graphite anodes (*E*(−)) were simultaneously monitored[34]. It was found that the potential of the graphite anode never fell below 0 V versus Li/Li⁺ even at −30 °C (Extended Data Fig. 6b), indicating a low overpotential at the anode and the consequent absence of Li plating. This is partially ascribed to the similar impedance between NMC811 cathode and graphite anodes at 25 °C (Extended Data Fig. 6c) and at −30 °C (Extended Data Fig. 4d). When the temperature is decreased from 25 °C to −30 °C, the SEI resistance R_{SEI} and charge transfer resistance R_{ct} of both the cathode and anode increase. The resistances of SEI and charge transfer for cathode and anode ($R_{SEI,cathode} = 4.8$, $R_{SEI,anode} = 5.6$, $R_{ct,cathode} = 22.5$ and $R_{ct,anode} = 25.2$) at 25 °C increased to $R_{SEI,cathode} = 72.3$, $R_{SEI,anode} = 81.5$, $R_{ct,cathode} = 228.5$ and $R_{ct,anode} = 241.2$ at −30 °C (Extended Data Fig. 6 and Supplementary Discussion 11). Importantly, the nearly identical impedance values of the cathode and anode at different temperatures indicate

that impedance matching was successfully achieved via tailoring the interphasial chemistry.

Characterization of the electrodes and interphasial chemistry

To identify the interphasial chemistry, the morphology and composition of the SEI on the graphite anode were systematically investigated. Under high-resolution transmission electron microscopy (HRTEM), a uniform and thin SEI of around 2 nm was observed on the graphite anode after 20 cycles in MDFA/MDFSA-based electrolyte (Fig. 4a). Such low thickness approaches the theoretical lower limit of an interphase, which reflects the effectiveness of the LiF-based interphases in insulating electron tunnelling. In contrast, a much thicker SEI layer of about 14 nm was observed for EC/DEC-based electrolytes (Fig. 4b). The roughness and thickness of the SEI were also studied by electrochemical atomic force microscopy (AFM). As shown in Fig. 4c–e, the pristine graphite particles have a smooth surface with a roughness of about 0.233 nm. In good agreement with the HRTEM observations, the roughness of the cycled graphite in the MDFA/MDFSA-based electrolyte obtained by AFM increased to about 3.0 nm (Fig. 4e), much smaller than the value of approximately 11.8 nm in the EC/DEC-based electrolyte (Fig. 4d). X-ray diffraction and scanning electron microscopy were also used to characterize the graphite anodes after 20 cycles at −30 °C (Supplementary Discussion 12).

To identify the chemical composition of the SEI on cycled graphite anodes, X-ray photoelectron spectroscopy (XPS) with an Ar⁺ sputtering depth profiling was performed. The elements and their related atomic

Article

ratios detected in the SEI on graphite recovered from 1 M LiTFSI MDFA/MDFSA–TTE electrolyte are summarized in Fig. 4f, and the C 1s and F 1s spectra are shown in Fig. 4g and Fig. 4h, respectively. The top surface of the SEI is composed of both organic (CO_2CF_2) and inorganic (LiF, Li_2CO_3) components. N and S are found in the SEI from MDFA/MDFSA-based electrolytes, which arise from the decomposition of the TFSI⁻ anion and MDFA co-solvent. In the C 1s spectra (Fig. 4g), the organic signals (C–O, $CO_2\underline{C}F_2$) drop to the noise level at 300 s of sputtering, whereas the LiF signal persists throughout the whole sputtering process (Fig. 4h). Combining the results from the C 1s and F 1s spectra, it is concluded that a robust bilayer SEI with LiF-rich inner layer and organic-rich outer layer was formed (Supplementary Discussion 13).

Characterization of the NMC811 cathode interphases also revealed the formation of a LiF-rich inner layer and an organic-rich outer layer CEI in the MDFA/MDFSA-based electrolyte (Supplementary Discussion 14). DFT calculations of reaction energies of MDFA, TTE and MDFSA on a four-layer slab model of Li_xNiO_2 (104) corroborate these observations. At high potentials, surface oxygens become highly reactive, and electrolyte species in contact with these surfaces are subject to dehydrogenation, which sets the upper limit on the anodic stability window. Here we found for the half-lithiated surface that dehydrogenation of MDFA without chemisorption of the radical on the CF_2 carbon is energetically favourable with a reaction energy of −0.49 eV with Perdew–Burke–Ernzerhof (PBE)+U and a similar energy of −0.45 eV using the SCAN functional (Extended Data Fig. 7a). Dehydrogenation of TTE on $Li_{0.5}NiO_2$ may also be possible, proceeding with a much smaller reaction energy of −0.05 eV with PBE+U. The reaction is somewhat more favourable when considering the SCAN functional, giving an energy of −0.31 eV (Extended Data Fig. 7b). Lastly, cluster calculations discussed previously predict Li⁺–MDFA reduction potentials in the range of 3.6 V to 4.0 V, corresponding to the loss of SO_2F products on the higher end of that range and direct defluorination on the lower end. The high reduction potentials computed for these reactions not only are relevant for SEI formation but also could factor into CEI formation at low state of charge or at open-circuit voltage when the cathode is in the discharged state. On $Li_{1.0}NiO_2$, PBE+U predicts a reaction energy of 0.50 eV for Li⁺–MDFSA to form the SO_2F product with a sizeable shift to −1.03 eV observed for the same configuration using SCAN (Extended Data Fig. 7c). A case is made in Supplementary Discussion 15 that the SCAN functional produces a more physically realistic description of the electronic structure, implying that decomposition of MDFSA may provide some degree of passivation on the cathode surface before cycling. Downstream decomposition of the SO_2F product is the most likely source of the thin LiF-rich layer in the inner part of the CEI with by-products of MDFA and TTE dehydrogenation and radical condensation comprising the fluorine-rich organic outer layer.

Conclusion

In this work, we reported an electrolyte design principle for high-energy batteries operating under extreme conditions. Central to this principle is the identification of solvents with a relatively low DN (less than 10) and high dielectric constant (greater than 5) values, which minimizes the Li⁺–solvent binding energy while still dissociating the lithium salt. Supplementing the electrolyte with a component with a high reduction potential enables the formation of similar LiF-rich interphases on both anodes and cathodes, facilitating similar lithiation/delithiation kinetics on both anodes and cathodes. The thermodynamic (capacity) and kinetics (impedance) match for anodes and cathodes render NMC811‖graphite batteries with the capabilities of fast charging and wide service temperature range without Li plating. As a proof of concept, a rationally designed 1 M LiTFSI MDFA/MDFSA–TTE electrolyte enables the formation of self-limiting LiF-rich interphases on anodes and cathodes, thus achieving the capacity and impedance matching

even under extreme conditions. The 4.5 V NMC811‖graphite full cells at a practical areal capacity of more than 2.5 mAh cm⁻² can effectively operate over a wide temperature range (−60 °C to +60 °C). Remarkably, practical pouch cells retain more than 83% room-temperature capacity over 300 cycles with an average CE of more than 99.9% at −30 °C. This design principle opens a direction for high-voltage, fast-charging and wide-temperature-operating batteries.

Online content

Any methods, additional references, Nature Portfolio reporting summaries, source data, extended data, supplementary information, acknowledgements, peer review information; details of author contributions and competing interests; and statements of data and code availability are available at https://doi.org/10.1038/s41586-022-05627-8.

1. Goodenough, J. B. & Kim, Y. Challenges for rechargeable Li batteries. *Chem. Mater.* **22**, 587–603 (2010).
2. Winter, M., Barnett, B. & Xu, K. Before Li ion batteries. *Chem. Rev.* **118**, 11433–11456 (2018).
3. Liu, Y., Zhu, Y. & Cui, Y. Challenges and opportunities towards fast-charging battery materials. *Nat. Energy* **4**, 540–550 (2019).
4. Rodrigues, M.-T. F. et al. A materials perspective on Li-ion batteries at extreme temperatures. *Nat. Energy* **2**, 17108 (2017).
5. Xu, K. Nonaqueous liquid electrolytes for lithium-based rechargeable batteries. *Chem. Rev.* **104**, 4303–4418 (2004).
6. Smart, M. et al. Improved low-temperature performance of lithium-ion cells with quaternary carbonate-based electrolytes. *J. Power Sources* **119**, 349–358 (2003).
7. Herreyre, S. et al. New Li-ion electrolytes for low temperature applications. *J. Power Sources* **97**, 576–580 (2001).
8. Dong, X., Guo, Z., Guo, Z., Wang, Y. & Xia, Y. Organic batteries operated at −70 °C. *Joule* **2**, 902–913 (2018).
9. Rustomji, C. S. et al. Liquefied gas electrolytes for electrochemical energy storage devices. *Science* **356**, eaal4263 (2017).
10. Holoubek, J. et al. Tailoring electrolyte solvation for Li metal batteries cycled at ultra-low temperature. *Nat. Energy* **6**, 303–313 (2021).
11. Zhang, S., Xu, K. & Jow, T. A new approach toward improved low temperature performance of Li-ion battery. *Electrochem. Commun.* **4**, 928–932 (2002).
12. Huang, C. K., Sakamoto, J., Wolfenstine, J. & Surampudi, S. The limits of low-temperature performance of Li-ion cells. *J. Electrochem. Soc.* **147**, 2893 (2000).
13. Zhang, S., Xu, K. & Jow, T. Low temperature performance of graphite electrode in Li-ion cells. *Electrochim. Acta* **48**, 241–246 (2002).
14. Petzl, M., Kasper, M. & Danzer, M. A. Lithium plating in a commercial lithium-ion battery—a low-temperature aging study. *J. Power Sources* **275**, 799–807 (2015).
15. Cai, W. et al. The boundary of lithium plating in graphite electrode for safe lithium-ion batteries. *Angew. Chem. Int. Ed.* **133**, 13117–13122 (2021).
16. Johnson, L. et al. The role of LiO_2 solubility in O_2 reduction in aprotic solvents and its consequences for Li–O_2 batteries. *Nat. Chem.* **6**, 1091–1099 (2014).
17. Burke, C. M., Pande, V., Khetan, A., Viswanathan, V. & McCloskey, B. D. Enhancing electrochemical intermediate solvation through electrolyte anion selection to increase nonaqueous Li–O_2 battery capacity. *Proc. Natl Acad. Sci. USA* **112**, 9293–9298 (2015).
18. Holoubek, J. et al. An all-fluorinated ester electrolyte for stable high-voltage Li metal batteries capable of ultra-low-temperature operation. *ACS Energy Lett.* **5**, 1438–1447 (2020).
19. Ihara, M. et al. Properties of carbon anodes and thermal stability in $LiPF_6$/methyl difluoroacetate electrolyte. *J. Electrochem. Soc.* **150**, A1476 (2003).
20. Cho, Y.-G. et al. Enabling the low-temperature cycling of NMC‖graphite pouch cells with an ester-based electrolyte. *ACS Energy Lett.* **6**, 2016–2023 (2021).
21. Henderson, W. A. Glyme–lithium salt phase behavior. *J. Phys. Chem. B* **110**, 13177–13183 (2006).
22. Chu, H. et al. Achieving three-dimensional lithium sulfide growth in lithium–sulfur batteries using high-donor-number anions. *Nat. Commun.* **10**, 188 (2019).
23. Linert, W., Camard, A., Armand, M. & Michot, C. Anions of low Lewis basicity for ionic solid state electrolytes. *Coord. Chem. Rev.* **226**, 137–141 (2002).
24. Li, Y., Lu, Y., Adelhelm, P., Titirici, M.-M. & Hu, Y.-S. Intercalation chemistry of graphite: alkali metal ions and beyond. *Chem. Soc. Rev.* **48**, 4655–4687 (2019).
25. Xue, W. et al. FSI-inspired solvent and "full fluorosulfonyl" electrolyte for 4 V class lithium-metal batteries. *Energy Environ. Sci.* **13**, 212–220 (2020).
26. Seo, D. M., Borodin, O., Han, S.-D., Boyle, P. D. & Henderson, W. A. Electrolyte solvation and ionic association II. Acetonitrile-lithium salt mixtures: highly dissociated salts. *J. Electrochem. Soc.* **159**, A1489 (2012).
27. Chen, J. et al. Electrolyte design for LiF-rich solid–electrolyte interfaces to enable high-performance microsized alloy anodes for batteries. *Nat. Energy* **5**, 386–397 (2020).
28. Bogle, X., Vazquez, R., Greenbaum, S., Cresce, A. V. W. & Xu, K. Understanding Li⁺–solvent interaction in nonaqueous carbonate electrolytes with ¹⁷O NMR. *J. Phys. Chem. Lett.* **4**, 1664–1668 (2013).
29. Chen, S. et al. High-voltage lithium-metal batteries enabled by localized high-concentration electrolytes. *Adv. Mater.* **30**, 1706102 (2018).
30. Ren, X. et al. Role of inner solvation sheath within salt–solvent complexes in tailoring electrode/electrolyte interphases for lithium metal batteries. *Proc. Natl Acad. Sci. USA* **117**, 28603–28613 (2020).

31. Zhang, X. et al. Advanced electrolytes for fast-charging high-voltage lithium-ion batteries in wide-temperature range. *Adv. Energy Mater.* **10**, 2000368 (2020).
32. Yamaki, J.-I. et al. Thermal studies of fluorinated ester as a novel candidate for electrolyte solvent of lithium metal anode rechargeable cells. *J. Power Sources* **102**, 288–293 (2001).
33. Beltrop, K. et al. Enabling bis(fluorosulfonyl)imide-based ionic liquid electrolytes for application in dual-ion batteries. *J. Power Sources* **373**, 193–202 (2018).
34. Waldmann, T. et al. Interplay of operational parameters on lithium deposition in lithium-ion cells: systematic measurements with reconstructed 3-electrode pouch full cells. *J. Electrochem. Soc.* **163**, A1232 (2016).

Article

Methods

Materials and electrolytes

MDFA, MDFSA, M4FP, EDFA and TTE were purchased from SynQuest Labs and used after being dehydrated with a 4-Å molecular sieve. LiTFSI, purchased from Gotion, was dissolved into mixed solvents (MDFA:MDFSA:TTE = 4:1:5, volume ratio) in predetermined concentrations in a glovebox filled with argon. The water content of the solution, as measured by a Karl Fischer aquameter, was 5 ppm or less. The solution of 1 M LiPF$_6$ in EC/DEC 50/50 (v/v), battery grade (Sigma), was used as received as a comparison. The ionic conductivities of the electrolytes were calculated from the high-frequency intercept of electrochemical impedance spectroscopy measured in symmetric Pt|Pt Swagelok blocking cells at various temperatures (−60 °C to +60 °C). Each sample subjected to DSC measurement was packed in a stainless steel pan, which was then crimp-sealed in a glovebox filled with argon. All of the DSC experiments were carried out at a cooling/heating rate of 5 °C min^{-1}.

A cathode coating of NMC811 (LiNi$_{0.8}$Mn$_{0.1}$Co$_{0.1}$O$_2$) on aluminium foil was provided by Saft America. These electrodes are composed of 94 wt% NMC811, 3 wt% carbon and 3 wt% polyvinylidene fluoride (PVDF), with approximately 30% porosity and 2.5 mAh cm^{-2} areal capacity (mass loading of about 11.5 mg cm^{-2}). Graphite powders within a narrow size distribution (3.5 ± 1.5 μm) were obtained from China Steel Chemical. Graphite electrodes were prepared by mixing graphite with carbon black and PVDF in a weight ratio of 92:2:6 using N-methyl pyrrolidinone as the solvent and were cast onto a copper foil, dried at 80 °C overnight under vacuum. The area capacity of graphite electrodes is 2.7 mAh cm^{-2}, corresponding to an N/P ratio of 1.08. These electrodes were cut into 1.2 cm^2 sheets and vacuum dried at 80 °C for 24 h before assembling.

Electrochemical measurements

CR2032 coin-type full cells were assembled by sandwiching Celgard 2325 as a separator between the graphite anodes and the NMC811 cathodes. For consistency, a fixed amount (40 μl) of liquid electrolyte was filled in all cells, and the Li-ion cells were formed at 0.2C between 2.5 V and 4.5 V for two cycles before testing. The cycling performance and rate capability of NMC811||graphite full cells with an areal capacity of 2.5 mAh cm^{-2} and an N/P ratio of 1.1 in different electrolytes were examined in the voltage range of 2.5–4.5 V. Cycling conditions for each test are described in the discussion section or figure captions. The C rate was determined by the charging time, for example, 1C equal to 1 h. As for the pouch cells, aluminium and nickel strips were attached as electrode tabs to the sides of the cathode and anode, respectively. All the electrodes, separators and liquid electrolytes were the same as those used in coin cells. All single-layer pouch cells (5 cm × 7 cm) were vacuum sealed in a dry room in Saft without electrolyte and then shipped to the University of Maryland for electrolyte infiltration. Various amounts of electrolytes (3.5 g Ah^{-1}, 3.0 g Ah^{-1} and 2.5 g Ah^{-1}) were injected into the package for comparison. As with the coin cells, the pouch full cells with the same N/P ratio of 1.1 and areal capacity of 2.5 mAh cm^{-2} were charged/discharged at the same temperatures in all tests. Impedance spectra of three-electrode cells were tested over the frequency range of 0.01–1000,000 Hz using pouch cells that incorporate a small piece of Li metal as the reference electrode.

Characterization

All the cycled samples were recovered from full cells using the electrodes described above and cycled for 20 cycles, washed by MDFA solvent, followed by characterizations of XPS, AFM, scanning electron microscopy (by a Hitachi SU-70 field emission scanning electron microscope), TEM (by a JEOL-JEM 2100F), X-ray diffraction and Fourier transform infrared spectroscopy. XPS experiments were carried out on a high-resolution Kratos AXIS 165 X-ray photoelectron spectrometer using monochromic Al Kα radiation. To avoid exposure to air and moisture, samples were transported from the glovebox to the XPS instrument directly. AFM was conducted to measure the thickness of the SEI layer with a Dimension ICON atomic force microscope set up inside an argon-filled glovebox. Raman spectra were collected with a Horiba Jobin Yvon Labram Aramis using a 532-nm diode-pumped solid-state laser between 3,000 cm^{-1} and 100 cm^{-1}, with all the samples sealed in a test glass tube. PDF characterization was performed at the 28-ID-2 beamline of the National Synchrotron Light Source II of Brookhaven National Laboratory, using a photon wavelength of 0.18475 Å. The raw data were integrated using Fit2D software[35], followed by intensity correction, background removal, and Fourier transform in PDFgetx3 to obtain the PDF data[36].

MD simulations

The MD simulation cell of LiTFSI in MDFA/MDFSA–TTE contained 330 MDFA, 75 MDFSA, 380 TTE and 96 LiTFSI, while LiTFSI in MDFA cells contained 1,100 MDFA and 96 LiTFSI. A polarizable force field APPLE&P with the previously developed LiTFSI, TTE parameters was used[37,38]. The Li$^+$(MDFA) and Li$^+$(MDFSA) interactions, solvent charges and polarizabilities were fit using methodology from previous work but utilizing MP2/aug-cc-pvTz to compute electrostatic potential on a grid around solvents to fit charges[39], PBE/6-31+G(d,p) to compute the Li$^+$ binding energy and polarizability on a grid around solvents and G4MP2 to calculate Li$^+$ binding energy to solvents for the most favourable geometries.

The length of equilibration and production runs, simulation temperatures, density and the number of independent simulated replicas are summarized in Extended Data Table 2. The equations of motions were solved with a time reversible (RESPA) integrator over the following time resolutions: (1) the contribution from bonds and angles to the forces were calculated at any 0.5 fs, (2) the contribution of dihedrals and non-bonded forces within 8-Å cut-off were updated at any 1.5 fs, and (3) the remainder of the forces (reciprocal space Ewald using $k = 8^3$ vectors and non-bonded forces within 12-A or 14-Å cut-off were updated at any 3 fs. A Nose–Hoover thermostat was used for temperature control with the associated frequency of 0.01 fs^{-1}. An archive (tar file) containing all input files including force field files needed to perform bulk MD simulations of LiTFSI in MDFA/MDFSA–TTE is included in Supplementary Information. A manual to file format used by the MD simulation code has been previously published as Supplementary Information[37].

Quantum chemistry calculations of Li$^+$ solvation

The Li$^+$(solvent) binding energies (shown in Fig. 1c) were calculated using DFT with wB97XD functional, 6-31+G(d,p) basis set with solvent and Li$^+$(solvate) immersed in implicit solvent that is modelled using PCM(ether) as implemented in Gaussian software package[40].

The reduction potential for the complexes of interest shown in Supplementary Fig. 2 denoted as complex A was calculated as the negative of the free energy of formation of A$^-$ in solution ($\Delta G^S_{298K} = G^S_{298K}(A^-) - G^S_{298K}(A)$) divided by Faraday's constant (F) as given by:

$$G^{red} = -\frac{\Delta G^S_{298K}}{F} - 1.4 \text{ V}$$

The difference between the Li$^+$/Li and absolute reduction potential of 1.4 V was subtracted to convert results to Li$^+$/Li scale as discussed extensively elsewhere[41].

Modelling of surface reactions

Calculations for the determination of reaction energies for decomposition reactions on a four-layer slab model of LiNiO$_2$ (104) were performed using VASP 5.4[42]. All structure optimizations were performed using PBE+U (U = 5.96 eV for Ni) and _sv and _pv potentials for Li and Ni, respectively[43]. Only the gamma point is considered for surface calculations. Single-point energies were also computed with the SCAN functional[44]. The plane-wave basis was expanded to 520 eV for PBE methods and

800 eV for SCAN. Dipole corrections were used in optimizations and single-point energy calculations as well. In calculations with Li$^+$–MDFA, a single F$^-$ ion was added elsewhere on the surface to neutralize the cell. The reactant state used here is the minimum energy physisorbed state. Calculations were prepared using the Atomic Simulation Environment and density of states were analysed with the VASP plugin in pymatgen[45,46]. Visuals were produced with VESTA[47].

Data availability

The data that support the findings of this study are available within this article and its Supplementary information. Additional data are available from the corresponding authors upon reasonable request.

35. Hammersley, A., Svensson, S., Hanfland, M., Fitch, A. & Hausermann, D. Two-dimensional detector software: from real detector to idealised image or two-theta scan. *High Pressure Res.* **14**, 235–248 (1996).
36. Qiu, X., Thompson, J. W. & Billinge, S. J. PDFgetX2: a GUI-driven program to obtain the pair distribution function from X-ray powder diffraction data. *J. Appl. Crystallogr.* **37**, 678 (2004).
37. Borodin, O. et al. Insights into the structure and transport of the lithium, sodium, magnesium, and zinc bis(trifluoromethansulfonyl)imide salts in ionic liquids. *J. Phys. Chem. C* **122**, 20108–20121 (2018).
38. Glaser, R., Borodin, O., Johnson, B. R., Jhulki, S. & Yushin, G. Minimizing long-chain polysulfide formation in Li–S batteries by using localized low concentration highly fluorinated electrolytes. *J. Electrochem. Soc.* **168**, 090543 (2021).
39. Borodin, O. & Smith, G. D. Quantum chemistry and molecular dynamics simulation study of dimethyl carbonate: ethylene carbonate electrolytes doped with LiPF$_6$. *J. Phys. Chem. B* **113**, 1763–1776 (2009).
40. Gaussian 16 Rev. C.01 (Gaussian Inc., Wallingford, CT, 2016).
41. Borodin, O. in *Electrolytes for Lithium and Lithium-Ion Batteries: Modern Aspects of Electrochemistry* Vol. 58 (eds Richard, T. et al.) 371–401 (Springer, 2014).
42. Jürgen, H. Ab-initio simulations of materials using VASP: density-functional theory and beyond. *J. Comput. Chem.* **29**, 2044–2078 (2008).
43. Dixit, M. et al. Thermodynamic and kinetic studies of LiNi$_{0.5}$Co$_{0.2}$Mn$_{0.3}$O$_2$ as a positive electrode material for Li-ion batteries using first principles. *Phys. Chem. Chem. Phys.* **18**, 6799–6812 (2016).
44. Sun, J., Ruzsinszky, A. & Perdew, J. P. Strongly constrained and appropriately normed semilocal density functional. *Phys. Rev. Lett.* **115**, 036402 (2015).
45. Larsen, A. H. et al. The atomic simulation environment—a Python library for working with atoms. *J. Phys. Condens. Matter* **29**, 273002 (2017).
46. Ong, S. P. et al. Python Materials Genomics (pymatgen): a robust, open-source Python library for materials analysis. *Comput. Mater. Sci.* **68**, 314–319 (2013).
47. Momma, K. & Izumi, F. VESTA 3 for three-dimensional visualization of crystal, volumetric and morphology data. *J. Appl. Crystallogr.* **44**, 1272–1276 (2011).

Author contributions J.X. and C.W. conceived the idea for the project. J.X., J.Z., H.W. and S.H. prepared the materials and performed electrochemical experiments. T.P.P., K.X. and O.B. conducted the quantum chemistry calculations and MD simulations. F.C. carried out the NMR analysis. J.L. and H.H. performed the AFM measurements. S.T., E.H. and X.-Q.Y. conducted the PDF experiments. All the authors discussed the results, analysed the data and drafted the manuscript.
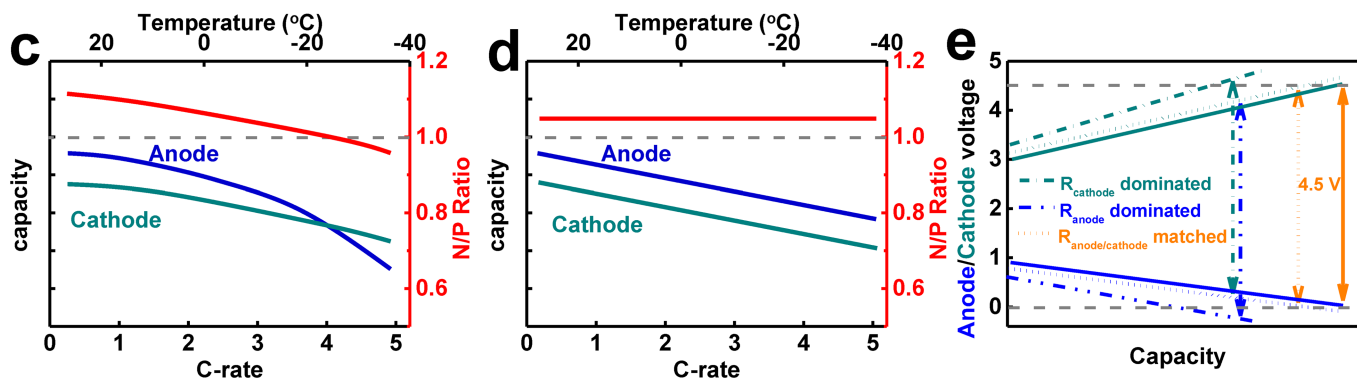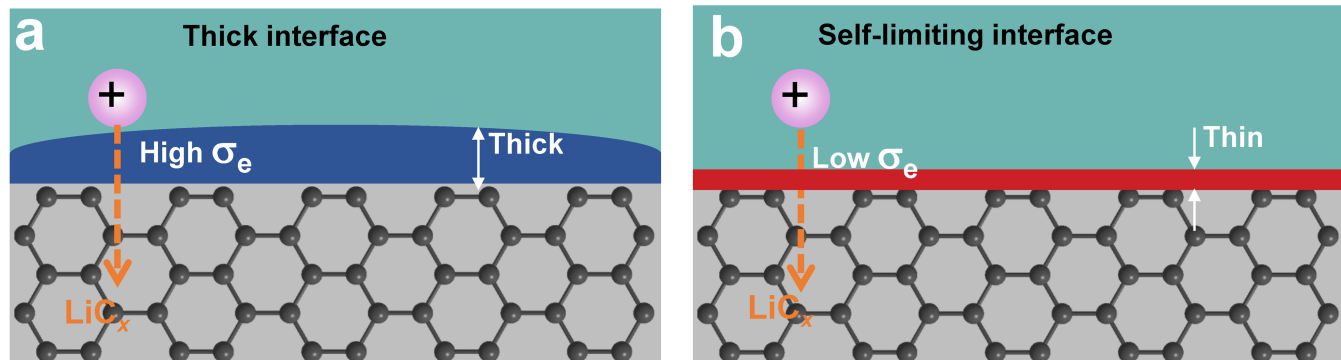
Extended Data Fig. 1 | Illustration of the capacity matching and kinetic matching. a, Thick interface between the commercial carbonate-based electrolyte and lithiated graphite anodes. **b**, Self-limiting interface between the designed electrolyte and lithiated graphite anodes. **c-e**, Schematic illustration of (**c**) capacity mismatching and (**d**) capacity matching as a function of charge rate or charge temperature, as well as (**e**) resistance matching between anode and cathode.
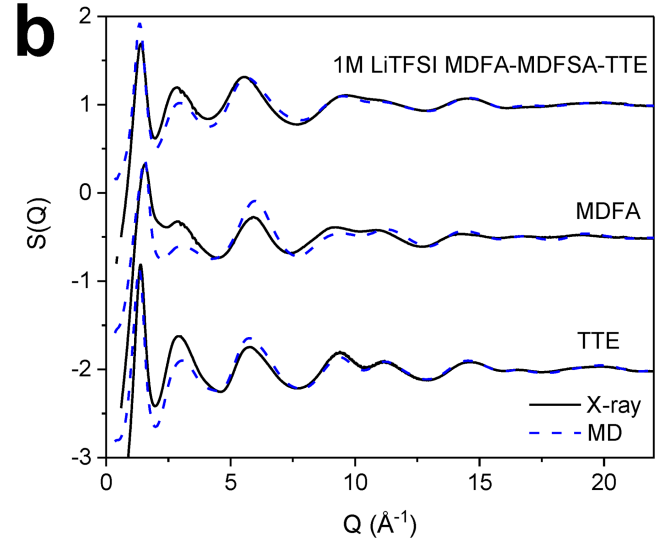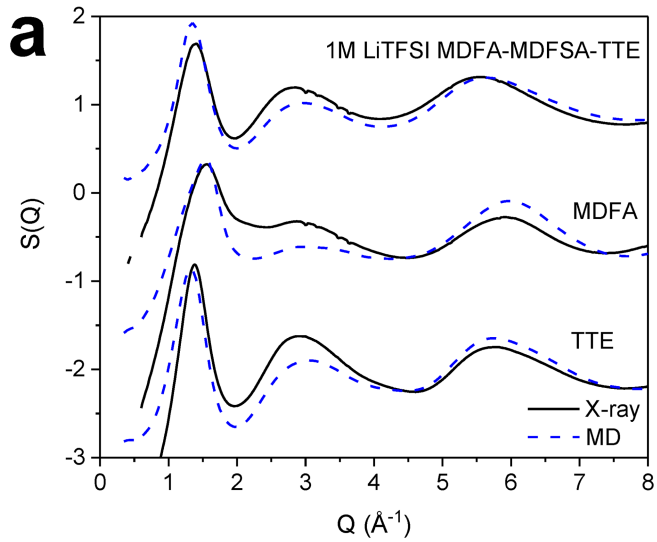
Extended Data Fig. 2 | X-ray measurements and MD simulation results.
a, b, A structure factor S(Q) from X-ray measurements (solid black line) and MD simulations (blue dash) for 1M LiTFSI in MDFA/MDFSA–TTE electrolyte and two dominating solvents MDFA and TTE. S(Q) for MDFA and TTE were shifted by −1.5 and 3.0.
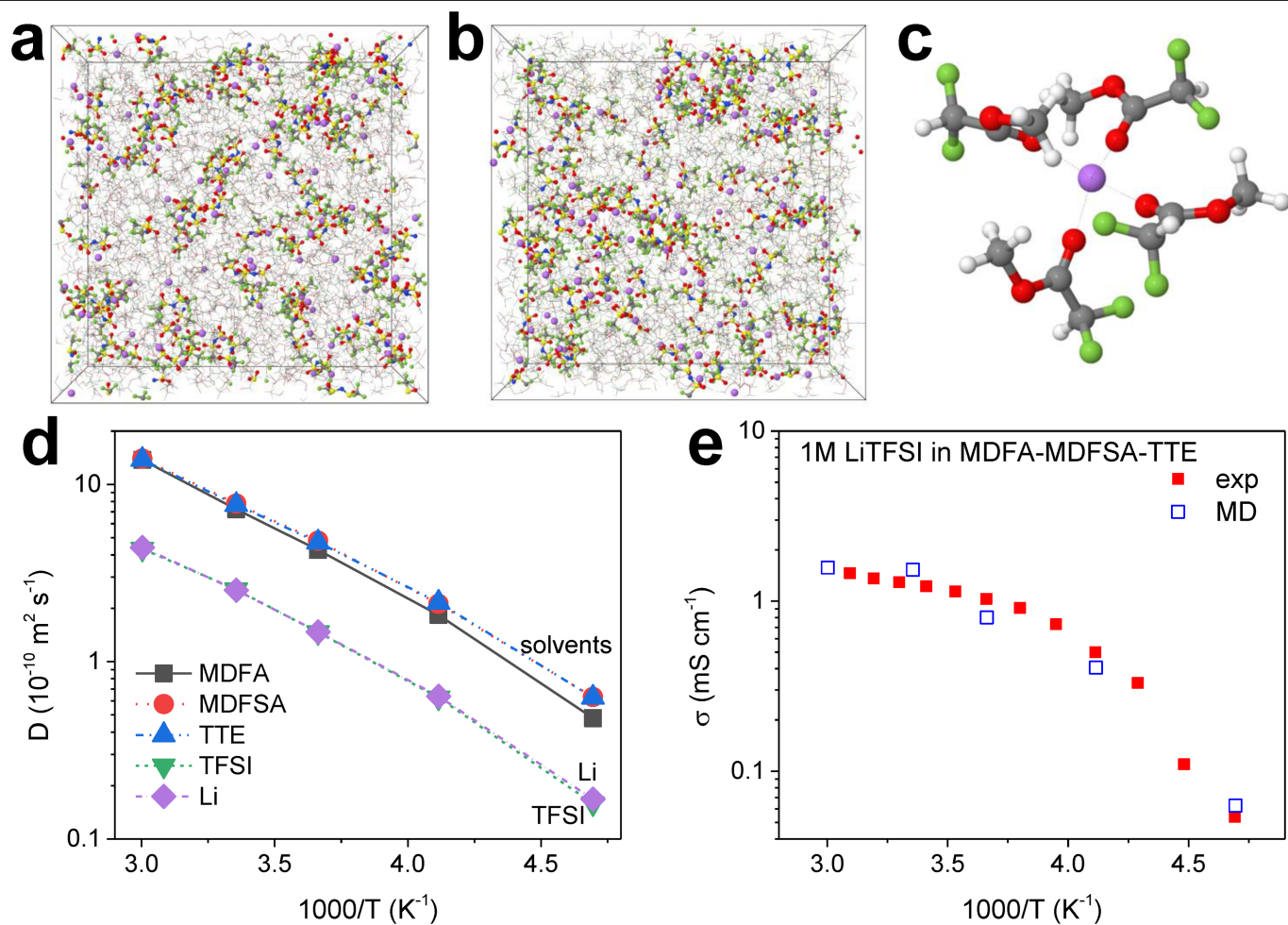
Extended Data Fig. 3 | MD simulation results. a, **b**, A snapshot of MD simulation box of LiTFSI in MDFA (**a**) and 1M LiTFSI in MDFA/MDFSA–TTE (**b**) from MD simulations at 25 °C. Solvent is shown as wireframe. **c**, Li⁺(MDFA)₄ free Li⁺ (solvent separated from TFSI⁻) from MD simulation of 1M LiTFSI in MDFA/ MDFSA–TTE (**b**, **c**) at 25 °C. Jmol colour scheme are used: Li – purple, N – blue,

F – green, S – yellow, C – grey, O – red, H – white. **d**, Ion and solvent self-diffusion coefficients from MD simulations of 1M LiTFSI in MDFA/MDFSA–TTE electrolyte. **e**, Conductivity of 1M LiTFSI in MDFA-MDFSA–TTE electrolyte from MD simulations and experiments.
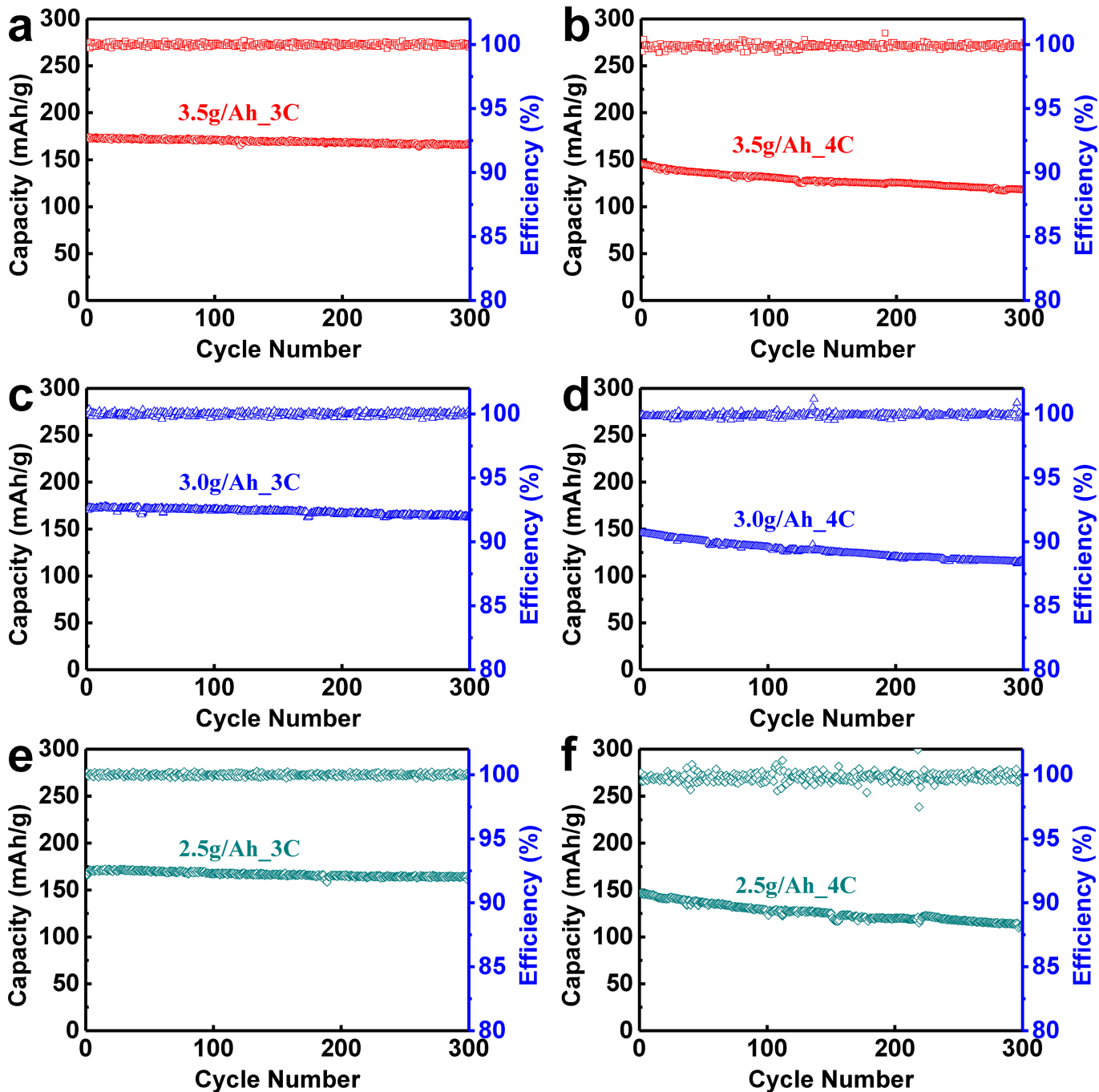
Extended Data Fig. 4 | Rate performance of polycrystalline NMC811‖graphite pouch cells at 25 °C. a-f, Pouch cells with different amount of 1M LiTFSI MDFA/MDFSA–TTE electrolyte under 3C (**a**, **c**, **e**), and 4C (**b**, **d**, **f**).
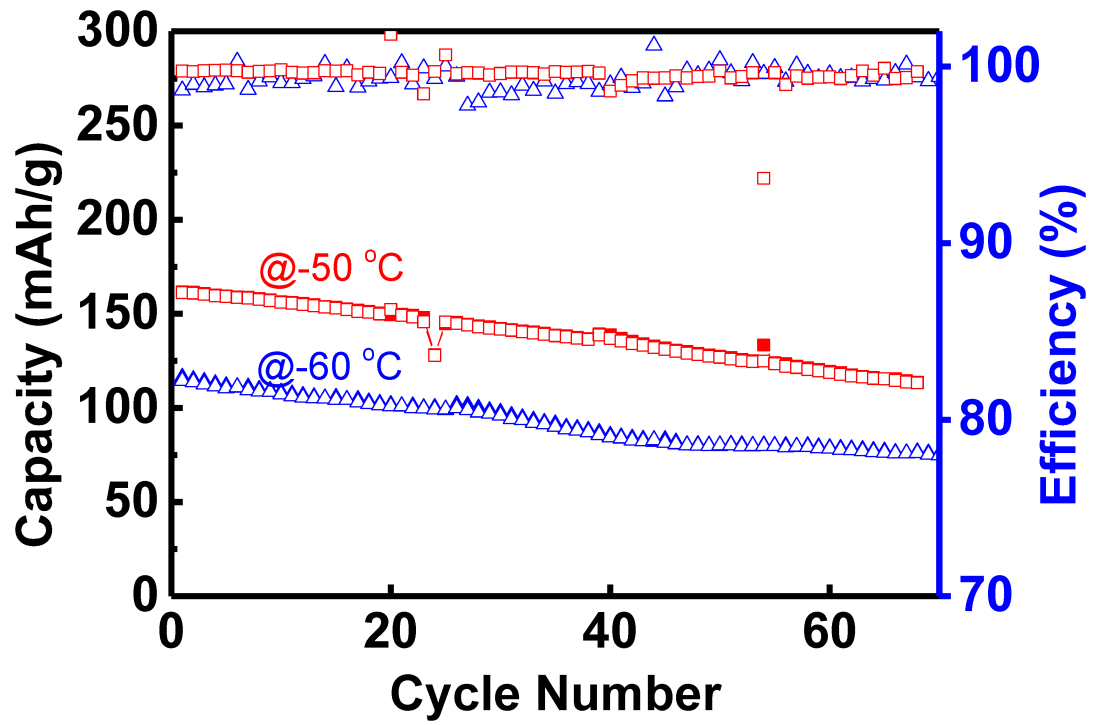
Extended Data Fig. 5 | Cycling performance at ultralow temperature. Cycling performance of NMC811||graphite full cells at 0.1C under −50/60 °C.

a

Anode: Graphite
RE: Li-metal
Cathode: NMC 811

E$_{(-)}$
E$_{(+)}$
U

3-electrode pouch cell

b

1M LiTFSI MDFA/MDFSA-TTE @ -30 °C

U & E$_{(+)}$ / V
E$_{(-)}$ / V vs. Li/Li$^+$
Time / h

c

1M LiTFSI MDFA/MDFSA-TTE @ 25 °C

R1   R3   R2   W1
CPE2   CPE1

■ Anode
● Cathode
▲ Full cell

-Z'' (ohm)
Z' (ohm)

d

1M LiTFSI MDFA/MDFSA-TTE @ -30 °C

■ Anode
● Cathode
▲ Full cell

-Z'' (ohm)
Z' (ohm)
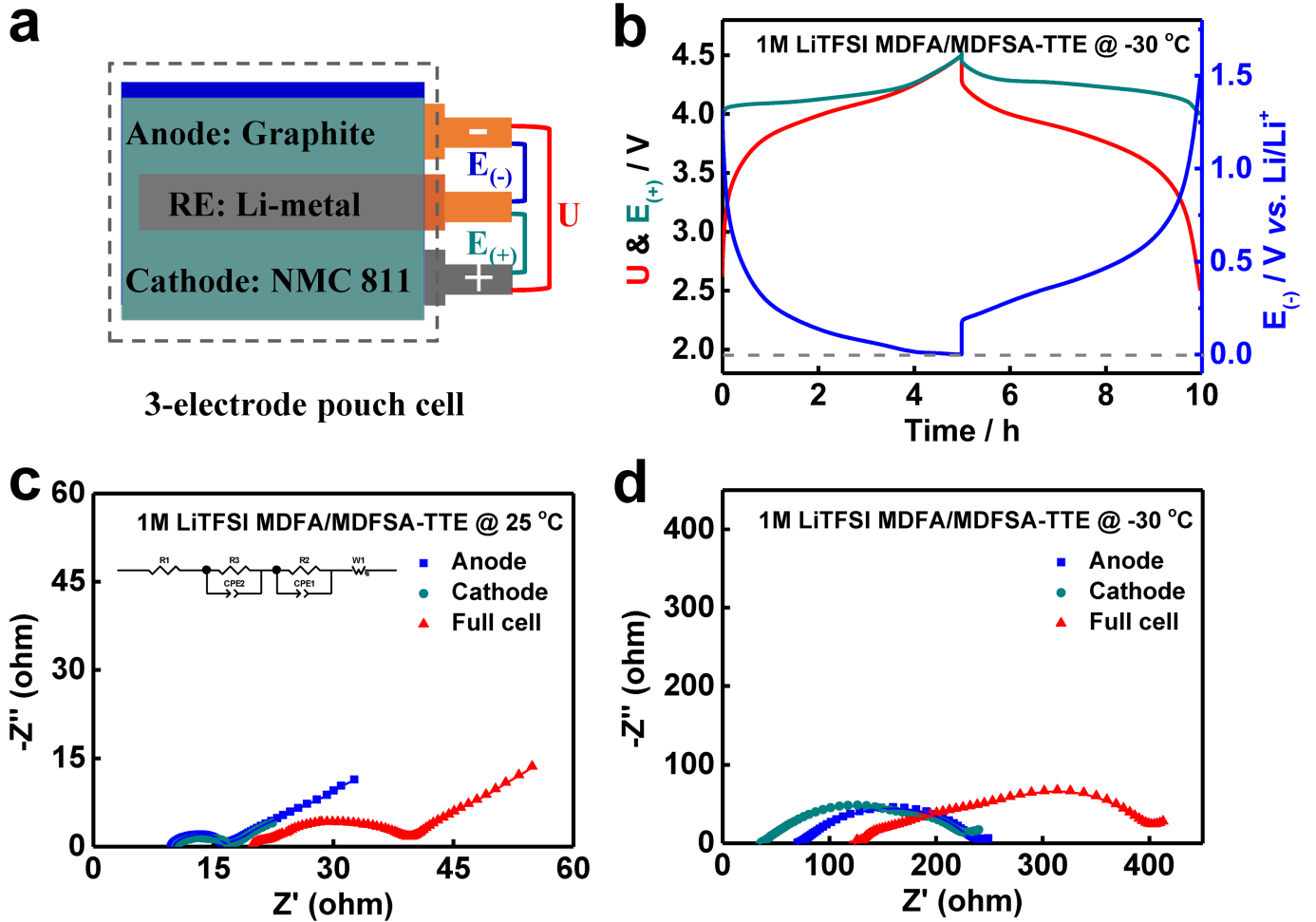
Extended Data Fig. 6 | Kinetic analysis of the low-temperature process. a, Cell illustration of three-electrode set up for kinetic analysis. **b**, Cell voltage and electrode potential of NMC811‖graphite pouch cells in 0.2C under −30 °C. **c**, **d**, Nyquist impedance plots and fitted lines using the equivalent circuit of the three-electrode cells containing 1M LiTFSI MDFA/MDFSA−TTE electrolyte at (**c**) 25 °C and (**d**) −30 °C. Impedance spectra were obtained at 50% SOC.
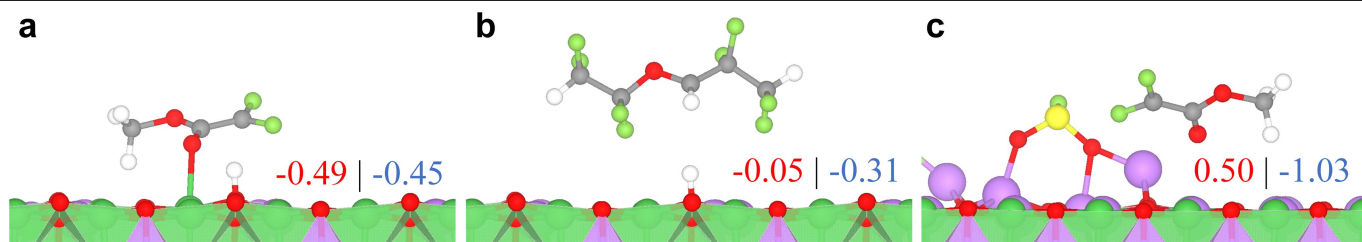
Extended Data Fig. 7 | DFT calculations of reaction energies. a-c, Reaction energies from PBE+U (red) and SCAN (blue) (units: eV) for dehydrogenation of MDFA on $Li_{0.5}NiO_2$ (**a**), TTE on $Li_{0.5}NiO_2$ (**b**), and Li^+-MDFSA on $Li_{1.0}NiO_2$ – a single F^- ion is present on the surface as well to neutralize the cell (**c**). Refer to text for explanation of the large energy difference in (**c**).

Extended Data Table 1 | Physical properties of organic solvents used for low-temperature batteries

Solvent	DN	Relative dielectric	T_m (°C)	T_b (°C)	Electrochemical Window (V)	Ref
Diethyl ether	19.2	4.3	-117	35	< 4.0	[10]
Ethyl acetate	17.1	6.0	-84	77	1.5~4.7	[8]
Methyl propionate	11.0	6.2	-88	79	< 4.3	[20]
EDFA	**9.0**	**9.2**	**<-90**	**99.2**	**< 4.3**	**This work**
MDFA	**8.4**	**10.1**	**<-90**	**86**	**< 5.0**	**This work**
M4FP	**6.3**	**8.3**	**-42**	**95**	**< 4.8**	**This work**
Difluoromethane	<1.0	14.2	-136	-52	< 5.0	[9]

Relative dielectric and DN values (in boldface) are determined from capacitance measurements and calorimetry, respectively.

Extended Data Table 2 | Summary of MD simulation equilibration and production runs

LiTFSI in MDFA-MDFSA-TTE				
Number of replicas	4	2	2	1	1
T (°C)	60	25	0	-30	-60
Equilibration runs (ns)	108	37	81.7	161.9	118
Production runs (ns)	651	200	398	335	224.1
Density (kg m^{-3})	1433	1491	1554	1578	1628

LiTFSI in MDFA	
Number of replicas	2	2
T (°C)	60	25
Equilibration runs (ns)	27.5	50.1
Production runs (ns)	301.0	450.2
Density (kg m^{-3})	1280	1335